Contents lists available at ScienceDirect

Bioactive Materials

Bioceramic scaffolds with triply periodic minimal surface architectures guide early-stage bone regeneration

Miaoda Shen [a,1], Yifan Li [a,1], Fengling Lu [b], Yahui Gou [c], Cheng Zhong [a], Shukun He [a], Chenchen Zhao [a], Guojing Yang [d], Lei Zhang [e], Xianyan Yang [b], Zhongru Gou [b,**], Sanzhong Xu [a,*]

[a] Department of Orthopedics, The First Affiliated Hospital, Zhejiang University School of Medicine, Hangzhou, 310003, China
[b] Bio-nanomaterials and Regenerative Medicine Research Division, Zhejiang-California International Nanosystem Institute, Zhejiang University, Hangzhou, 310058, China
[c] Zhejiang University-University of Edinburgh Institute, Zhejiang University, Haining, 314499, China
[d] Department of Orthopaedics, The Third Hospital Affiliated to Wenzhou Medical University & Rui'an People's Hospital, Rui'an, 325200, China
[e] Department of Orthopaedics, The First Affiliated Hospital of Wenzhou Medical University, Wenzhou, 325000, China

ARTICLE INFO

ABSTRACT

The pore architecture of porous scaffolds is a critical factor in osteogenesis, but it is a challenge to precisely configure strut-based scaffolds because of the inevitable filament corner and pore geometry deformation. This study provides a pore architecture tailoring strategy in which a series of Mg-doped wollastonite scaffolds with fully interconnected pore networks and curved pore architectures called triply periodic minimal surfaces (TPMS), which are similar to cancellous bone, are fabricated by a digital light processing technique. The sheet-TPMS pore geometries (s-Diamond, s-Gyroid) contribute to a 3–4-fold higher initial compressive strength and 20%–40% faster Mg-ion-release rate compared to the other-TPMS scaffolds, including Diamond, Gyroid, and the Schoen's I-graph-Wrapped Package (IWP) *in vitro*. However, we found that Gyroid and Diamond pore scaffolds can significantly induce osteogenic differentiation of bone marrow mesenchymal stem cells (BMSCs). Analyses of rabbit experiments *in vivo* show that the regeneration of bone tissue in the sheet-TPMS pore geometry is delayed; on the other hand, Diamond and Gyroid pore scaffolds show notable neo-bone tissue in the center pore regions during the early stages (3–5 weeks) and the bone tissue uniformly fills the whole porous network after 7 weeks. Collectively, the design methods in this study provide an important perspective for optimizing the pore architecture design of bioceramic scaffolds to accelerate the rate of osteogenesis and promote the clinical translation of bioceramic scaffolds in the repair of bone defects.

1. Introduction

Pore geometry has gained increased attention in bone regenerative medicine because of its significance in determining the early-stage bone regeneration efficiency and long-term structural stability of porous scaffolds [1–5]. Generally, pore dimensions and interconnections are critical variables that determine the processes of cell migration, bone formation, and vascularization, in addition to the mechanical tolerance of biomaterials [6,7]. Although the effects of pore structural parameters on the angiogenesis and osteogenesis of porous scaffolds have been explored in various studies [8–10], it is difficult to prepare scaffolds with traditional additive manufacturing techniques to precisely tune pore architectures (geometry, size, curvature, etc.) to meet the corresponding requirements [11–13]. In particular, the existing knowledge involving early bone tissue ingrowth in porous networks could not provide a general standard for the production of biomimetic porous scaffolds for clinical translation.

Porous scaffolds must be carefully developed and optimized because pore architectures and surfaces have a significant impact on critical tissue regeneration parameters, such as nutrient transport, cell

migration, and new bone deposition [14–16]. As a result, the creation and refinement of pore designs based on tissue regeneration requirements are becoming an iterative process in scaffold design. It is known that the structure of the inorganic component of cancellous bone, hydroxyapatite (HA), is inherently heterogeneous and anisotropic. Some attempts have focused on the reproduction of the trabecular architectures of native bone, but customizing scaffold architecture to better fit competing criteria, such as structural, mechanical, and biological requirements, is still a difficulty [17–20].

Three-dimensional (3D) printing has been developed to fabricate porous biomaterials for customized reconstructive prostheses [21,22]. Extrusion-based printing techniques, such as robocasting and fused deposition modeling, usually produce scaffolds with regular and straight rods and scaffolds with noncurved pore walls [23–25]. Recently, the digital light processing (DLP) technique has been increasingly used in bone regeneration scaffolds to achieve complex cell units as it circumvents the geometric limitations of extrusion-based techniques [26]. An advanced DLP technique has been developed to prepare more ideal porous polymer and bioceramic scaffolds with a better control of the pore geometry features [27–30]. For instance, Charbonnier et al. [31] proposed a porous bioceramic manufacturing process that involved impregnating a 3D-printed wax mold. This process preserved the biocompatibility of phases, permitted homogeneous shrinkage of the biomaterial during heat treatment, and allowed for the reproducible and precise manufacturing of custom architectures. Zhang et al. [32] developed bioceramic scaffolds with hierarchical Haversian structures that benefitted multicellular delivery by inducing angiogenic and accelerated bone tissue ingrowth. In short, the remarkable advantage of this scaffold fabrication technique is that it can produce biomaterials with precisely controlled pore curvatures and complex shapes, such as a triply periodic minimal surface (TPMS) [33–36]. Some researchers have extensively studied TPMS pore geometries in porous metal and alloy bone grafts. A TPMS-based structure can be produced either by thickening the minimal surface to form sheet-based structures (S-Diamond and S-Gyroid pore geometries) or by solidifying the volumes enclosed by the TPMSs to form skeletal-based structures (Diamond, Gyroid, and IWP pore geometries) [35–37]. Many TPMS geometries of metallic and ceramic biomaterials resemble trabecular bone with a mean curvature close to zero, allowing the yield strengths and Young's moduli of these geometries to be compromised simultaneously to generate the expected biomechanical tolerance behaviors in bone tissue environments [29,38,39]. Therefore, TPMS scaffolds are expected to improve the biocompatibility and osteoconductivity of biomaterials and thus provide a new approach to the design of scaffolds for bone regeneration. Theoretically, it is an ideal geometry for bone regeneration materials. However, the influence of TPMS pore geometries on the mechanical properties and bone tissue ingrowth behavior of bioceramic scaffolds *in vivo* has received little attention.

In this study, we aimed to fabricate a series of bioceramic scaffolds with curved pore walls by using DLP-based 3D printing and to explore their potential in bone regeneration and repair applications. The nonstoichiometric wollastonite (6% Mg substituting Ca) bioceramic was used as the raw material to produce porous scaffolds because of its excellent mechanical properties compared to pure wollastonite and other calcium phosphate bioceramics [40,41]. For the first time, we compared the relationship between the early-stage osteoconductive behavior of bioceramics and a series of scaffolds with uncommon TPMS pore architectures (e.g., Diamond, s-Diamond, Gyroid, s-Gyroid, and IWP). The pore structure parameters, such as pore size, porosity, and specific volume ratio, were designed and characterized by computer-aided calculations. The effect of TPMS pore geometry on mechanical properties was demonstrated through mechanical measurement. The cell viability, cell proliferation, and osteogenic differentiation of bone marrow mesenchymal stem cells (BMSCs) on TPMS pore scaffolds were studied by cell testing *in vitro*. The bone regeneration ability in the early stage (3–10 weeks) *in vivo* was further investigated by

implanting the scaffolds into critical-sized femoral bone defects in rabbits. New bone regeneration and ingrowth were evaluated systematically with μCT and histological analysis. In summary, this is the first study to evaluate a range of TPMS pore geometries *in situ* in the living bone defect model to mediate and accelerate bone regeneration.

2. Materials and methods

2.1. Digital light processing 3D printing of bioceramic scaffolds

The reagent-grade inorganic salts that served as the raw materials for the bioceramics were provided by Sinopharm Reagent Co., Shanghai. Briefly, nonstoichiometric wollastonite powders (6% Mg-substituting wollastonite; CSi–Mg6) were synthesized by a wet-chemical precipitation process [40]. The morphology and crystallinity of powders were verified by an X-ray diffractometer (XRD; Rigaku D/max-rA, Japan). The powders were then ground by using zirconia balls submerged in ethanol (100 mL) in a ball mill (40 g powder and 120 g milling balls of 8 mm in diameter) for 6 h to obtain superfine powders (<5 μm in particle size).

The bioceramic slurry employed in the stereolithography for layer-by-layer (LbL) digital light printing of the porous scaffolds (Fig. 1A) consisted of self-prepared photosensitive resin and bioceramic powders with a resin/powder ratio of 2:3. The resin was mainly composed of 1,6-hexanediol diacrylate (HDDA) and 1,1,1-trimethylolpropane triacrylate (TMPTA) with the addition of 1 wt% diphenyl(2,4,6-trimethylbenzoyl) phosphine oxide (TPO), photoinitiator (relative to the total resin mass), and 2 wt% KOS110 dispersants (relative to the total powder mass). Five groups of cylindrical models with 3D periodic porous architectures with standard primitives, such as Diamond and Gyroid without and with sheet structure (s-Diamond, s-Gyroid) and IWP curve-surface pores (Fig. 1B), were designed by MathMod (ParisoLab Inc., Canada), Magics 21 (Materialise, Belgium), and Avizo (FEI Visualization Sciences Group, Lyon) software according to the methodology provided in previous literatures [42,43]. The flow of calculating the pore distribution of cell units using Avizo software was sown in Fig. S1. The printing procedures were carried out according to the conditions described previously [29]. The dimensions of the scaffolds were theoretically cylindrical, with a diameter of 6 mm and a height of 8 mm. The porosity and average pore size were constructed identically (~58% and ~800 μm) for five groups of porous scaffolds. The printed bodies were made with DLP technology, implementing stereolithography equipment (AUTOCERA-M, Beijing Ten Dimensions Technology Co., Ltd., China) to photopolymerize a resin and bioceramic powder mixture. The printed samples were washed with deionized water three times to remove uncured resins and then dried at 80 °C. Finally, the porous bodies were sintered at 1150 °C for 2 h in an air environment with a heating rate of 2 °C/min. The linear shrinkages of scaffolds with different pore geometries were not significantly different, and the actual dimensions after sintering were also similar because of the consistency of the bioceramic powders resulting from the preparation process.

2.2. Primary structure analysis

A mobile phone camera was used to record the external scaffold morphology and pore structures. Field-emission scanning electron microscopy (SEM; JEM-6700 F, Japan) was used to observe the microstructures of bioceramic scaffolds covered with a thin coating of gold. A digital Vernier caliper was used to measure the diameter (D) and height (H) of the cylindrical scaffolds before and after sintering to calculate the linear shrinkage.

2.3. Mechanical analysis

Compressive strength and elastic modulus tests were performed to evaluate the mechanical properties of the 6 sets of as-sintered cylindrical scaffolds (n = 6, Ø ~6 × 8.0 mm) according to the ASTM D695-02a
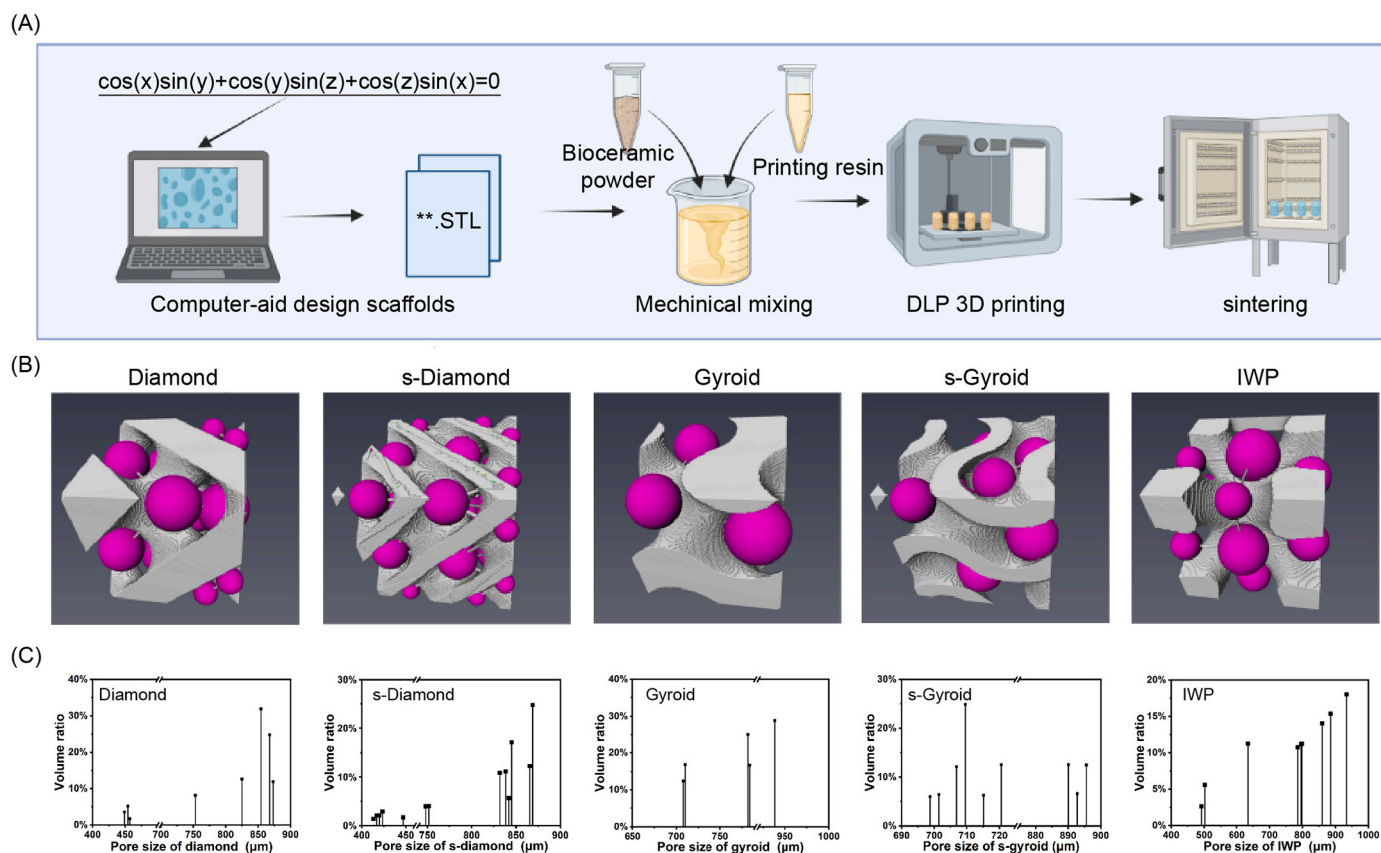
Fig. 1. Preparation procedures and primary characterization of porous Ca-silicate bioceramic scaffolds. (A) Schematic illustration of the fabrication of bioceramic scaffolds via DLP 3D printing (Created with BioRender.com); (B) 3D definition of the pore size via the maximum diameter of a virtual microsphere fitting within the pore architecture at any given point within the pore space; (C) Pore size distribution of the pore architecture in a unit cell of 3D models with five types of pore geometries.

standard with an Instron 5566 universal testing machine. Compressive strength testing was performed using a 10 kN load cell with a crosshead displacement speed of 0.5 mm/min. The elastic modulus was determined from the linear portion of the stress-strain curve.

2.4. Biodegradation testing in vitro

The cylindrical samples with varied pore geometries (m_0; n = 6) were separately weighed and soaked in Tris-HCl buffer (0.05 M; pH ~7.4) and SBF buffer (SL6710, Coolaber, Beijing, China) with a scaffold/buffer ratio of 1.0 g/50 mL at 37 °C. Twenty percent of the solution was swapped with an equal amount of fresh buffer each week. After immersing in the buffer for 2, 4, 6, 8, 12, and 14 days, the buffer (1.0 mL) was extracted and diluted tenfold in 2% HCl solution for examination of the ionic release concentrations of Ca, Si, Mg, and P (only in SBF buffer) by inductively coupled plasma measurement (ICP; Thermo, USA), and equivalent fresh buffer was added into the immersion medium. After 4 and 8 weeks of immersion, the samples were obtained from the Tris-HCl buffer at the predetermined time point, washed with deionized water and ethanol, and dried to a constant mass (m_t). The expression of mass decrease was as follows:

$$mass\ decrease = m_t/m_0 \times 100\%$$

2.5. Cell testing in vitro

2.5.1. Cell culture
BMSCs were used for the study. BMSCs were isolated from the

femoral bone marrow of 4-week-old C57BL/6 mice and cultured in a high-glucose Dulbecco's Modified Eagle's Medium (DMEM, Gibco, USA) supplemented with the 10% fetal bovine serum (FBS, Gibco, USA) and 1% penicillin/streptomycin (Gibco, USA) in a 5% CO_2 humidified atmosphere at 37 °C. The culture medium was replaced every two days.

2.5.2. Cell proliferation testing
BMSCs were seeded onto the scaffolds at a density of 1×10^3 cells/L in a 96-well plate. Cells incubated in a culture medium were used as the control. A cell counting kit-8 (CCK-8; Biosharp, China) was used to determine cell proliferation after 1, 3, and 7 days of culture. 10 μL CCK-8 solution was added to each well, followed by incubation at 37 °C for 2 h. Lastly, 100 μL of the supernatant was transferred to a 96-well plate and the absorbance at 450 nm was measured using a Multi-Mode microplate reader (SpectraMax i3x, Molecular Devices, CA) to detect cell proliferation.

2.5.3. Osteogenic differentiation testing
To test the effects of different TPMS scaffolds on the osteogenic differentiation of BMSCs, cells were seeded on scaffolds and cultured for 7 days to extract proteins and total RNA. The expression levels of osteogenesis-related proteins (OPN and Runx-2) and genes (OPN and Runx-2) in BMSCs were tested by Western blot and real-time polymerase chain reaction (RT-PCR), respectively. The culture medium (Control) was designed as the negative control. Primer sequences used in the RT-PCR were supplied in Table S1.

2.5.4. Cell viability testing
To test the effects of different TPMS scaffolds on the viability of

BMSCs, cells were seeded on scaffolds and cultured for 24 h. Living cells and dead cells were detected using Calcein/PI Live/Dead Viability/Cytotoxicity Assay Kit (C2015 M, Beyotime, China) in accordance with the manufacturer's instructions. Then, the cells were observed under a fluorescence microscopy (IX73, Olympus, Japan).

2.5.5. Immunofluorescence staining

After culturing for 7 days, cells were fixed in a 4% neutral formaldehyde solution for 15 min, permeabilized and incubated in a Quick-Block™ Blocking Buffer (Beyotime, China) for Immunol Staining for 15min. The cells were treated with OPN (1:500) overnight at 4 °C and then incubated with the secondary antibody anti-rabbit IgG for 1 h at room temperature. F-actin was used to stain the cytoskeleton (green) for 1 h at room temperature. DAPI was used to stain the nuclei (blue) for 15 min at room temperature, and the cells were then gently washed with PBS. Finally, the cells on different samples were detected by a confocal laser scanning microscope (FV3000, Olympus, Japan) to observe the expression of OPN.

2.6. Implantation of scaffolds in rabbit distal femur defects

2.6.1. Animals

The animal care techniques and experimental protocols in this study were reviewed and approved by the Animal Care and Use Committee of Zhejiang University. The distal femur defect models were mature male New Zealand rabbits (2.75–3.00 kg in mass; 3–4 months in age). This study adhered to the Animal Research: Reporting of *in vivo* experiments guidelines (ARRIVE) [44]. All rabbits were divided randomly into the five groups including Diamond, s-Diamond, Gyroid, s-Gyroid, and IWP scaffolds implantation.

2.6.2. Operative phase

Rabbits were fixed in the supine position on the surgical table and then anesthetized preoperatively with an intravenous injection of 3% sodium pentobarbital (Sigma–Aldrich Co.) at a dose of 1.0 mL/kg. Then, a critical-sized cylindrical defect (Ø ~6 × 8.0 mm) was created by a dental drill inserted into both lateral femoral condyles of each animal, and the porous scaffolds were implanted into the bone defect. The defect area was rinsed and washed carefully with 0.9% normal saline during the drilling process to remove wear particles, reduce drilling temperature, and avoid osteonecrosis. Finally, the muscles, tendons, and skin were sutured layer-by-layer with a Jinhuan Medical® suture 3–0. A daily injection of 800,000 units of penicillin G (800,000 U) was administered intramuscularly to all rabbits for five consecutive days to prevent postoperative infections. The rabbits were euthanized by excessive anesthesia at the end of weeks 3, 5, 7, and 10. Then, distal femur bone specimens were collected with a high-speed drill, and all excess soft tissue was removed.

2.7. μCT analysis

The bone defects were evaluated by microcomputed tomography (μCT) measurement (Inveon CT scanner, Siemens, Germany) with a voltage of 90 kV and a current of 55.6 μA. The sample data obtained by μCT scanning were converted to 3D images by 3D reconstruction software (VGStudio MAX, USA). The following tissue regeneration data of 3D-reconstructed μCT images were measured and calculated: the ratio of bone volume to the total defect volume (BV/TV), the ratio of residual material volume to the total defect volume (RV/TV), and the trabecular number (Tb·N).

2.8. Histological evaluation

Histological evaluation was used to analyze bone regeneration. The extracted specimens for undecalcified histological staining were fixed in 10% buffered formalin for over 7 days at 4 °C before being rinsed

overnight with tap water. All of the specimens were dehydrated in successive concentrations of ethanol solutions (70%, 80%, 95%, 98%, 100%) and cleaned with xylene. Afterward, the specimens were embedded in polymethylmethacrylate (PMMA) resin to prepare hard histological sections. As the specimens embedded in PMMA hardened, they were cut into 1000-μm-thick sections along the axis of the cylindrical bone defects with a sawing microtome (Leica 1600, Germany). The slices were then adhered to plastic support and polished to a thickness of approximately 100 μm. The samples were then stained with McNeal's staining and H&E staining. Afterward, they were observed by an optical microscope (DMLA, Leica; Germany) with different magnifications (40 × , 200 ×). The pictures of sections with a magnification of 40 were analyzed by the imaging analytical software Image-Pro Plus 6.0 (Media Cybernetic, USA). Both the newly formed bone surface area (BS) and the total surface area (TS) were quantitatively measured, and then the BS/TS was calculated to form the collected data (n = 3).

2.9. Statistical analysis

All statistical analyses were performed by the SPSS 25.0 statistical package (IBM, Armonk, USA). The data were expressed as the mean ± standard deviation (SD) and were analyzed with one-way ANOVA and post hoc Student–Newman–Keuls test. The results were considered statistically significant when they had a p-value less than 0.05. Graphs were prepared in Origin Pro 2022b (Northampton, USA) and GraphPad Prism v.9.0.0 (San Diego, USA).

3. Results

3.1. Primary characterization of powders and scaffolds

XRD patterns (Fig. S2) confirmed that the CSi–Mg6 powder and sintered scaffolds were both low-temperature β-phase wollastonite (PDF #43–1460). The porous samples showed similar linear shrinkage (19.2%–21.3%, $p < 0.05$), but other deformation was not observed from the scaffolds after sintering. The calculation of the initial average pore size or diameter of the interconnected pores (~800 μm) and porosity (~58%) was used to design computer-aided design (CAD) models that represented the five types of porous architectures. We calculated the actual porosity of all porous scaffolds with the mathematical formulas for the volume fraction of solids (dry-weighed samples) in Table 1. The porosity of the sintered scaffolds was 3%–7% less than the designed values (~58%). Meanwhile, CAD analysis demonstrated that the sheet-type pore geometries (s-Diamond, s-Gyroid) contribute to an increase in the specific surface area (surface area-to-volume ratio). Furthermore, the pore size distribution of the modeled structures was somewhat variable among the five groups of scaffolds (Fig. 1B), which was mostly due to the various curvature features and interconnected pore sizes (Fig. 1C).

3.2. Structural characterization of porous scaffolds

DLP-based 3D printing technology was used for the flexible printing of CSi–Mg6 scaffolds with various internal curved pore topologies (Fig. 2A and B). As the optical images (Fig. 2C) showed, the cylindrical morphology and pore architectures of scaffolds with carefully specified

Table 1
Porosity and surface to volume ratio of TPMS scaffolds.

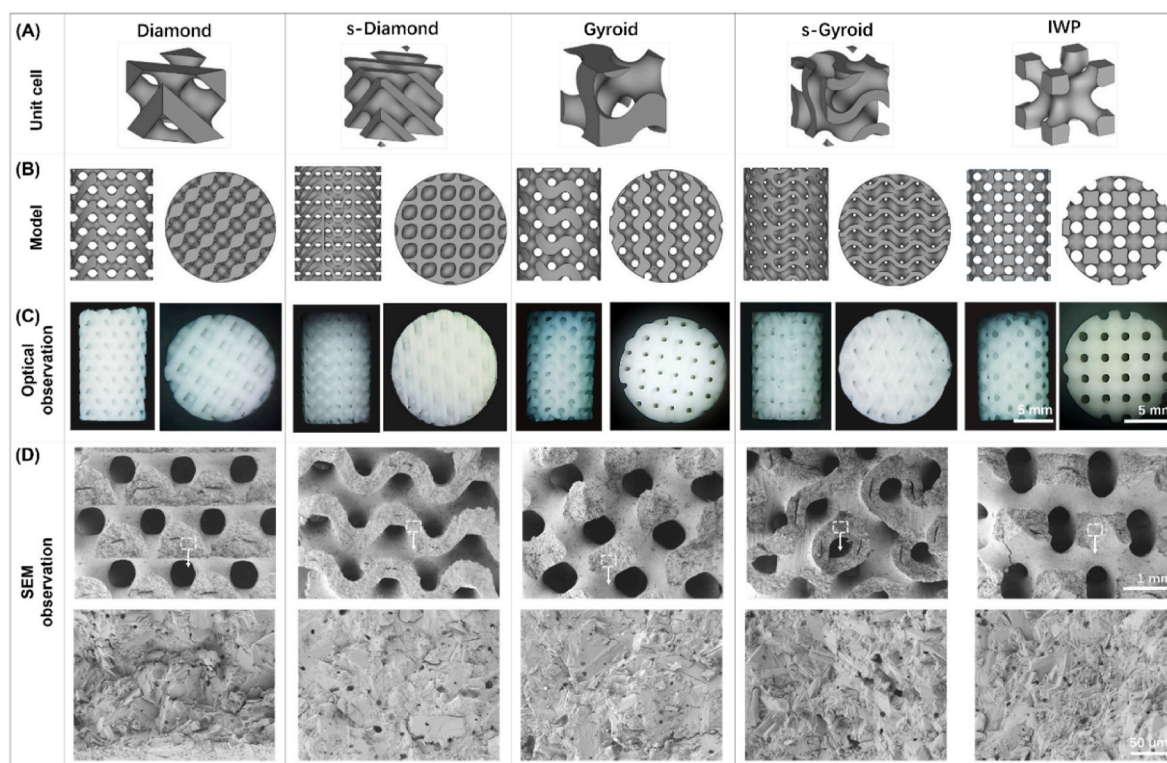| Geometry parameter	Diamond	s-Diamond	Gyroid	s-Gyroid	IWP
Porosity (%)	53.7 ± 2.2	50.5 ± 2.3	54.6 ± 1.9	50.4 ± 2.4	54.5 ± 1.7
Surface to volume ratio (1/mm)	6.4	9.1	6.4	8.9	6.1

Fig. 2. The morphological and structural characterization of the CSi–Mg6 scaffolds with five pore architectures. (A) The unit cell of the pore geometry; (B) Side- and top-view of the CAD models; (C) Optical images of the sintered scaffolds; (D) The SEM images and an enlarged view of the marked area showing the uniformity of the pore structure and the pore wall microstructures.

pore geometries were not easily changed after sintering. In particular, the full pore interconnectivity from the lateral view could be observed for all bioceramic scaffolds. The SEM images (Fig. 2D) also showed that the pore geometries in the fracture surface of sintered scaffolds were compatible with the intended porous models without an apparent deformation of the entire structure. It is worth mentioning that the pore walls showed similar surface microstructures and densification, mainly because of their identical chemical compositions and sintering conditions.

3.3. Effects of pore geometry on mechanical and bio-dissolution behavior in vitro

In Fig. 3A–E, we illustrate the representative stress-strain curves for the scaffolds under compression. For the s-Diamond and s-Gyroid scaffolds, the elastic stress increased almost linearly with shear strain in the initial two low-strain regions (regions S1 and S2), indicating that the scaffolds had an elastic response to the deformation. The stress continued to rise until it reached its peak stress (i.e., strength), at which time all of the pore walls shattered (region S3) because the fractured
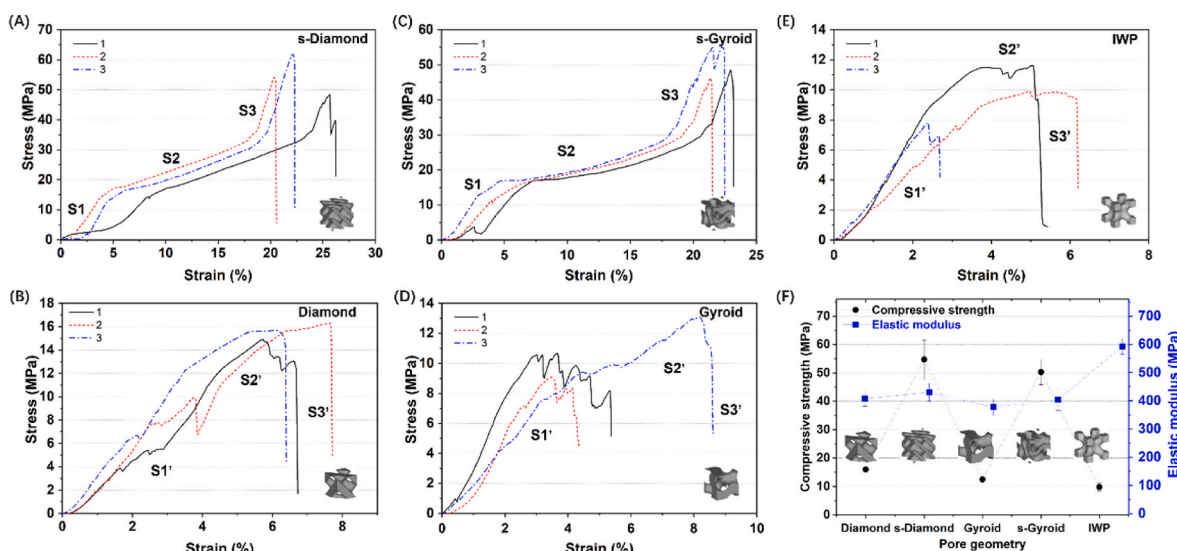

Fig. 3. Mechanical properties of the bioceramic scaffolds with different pore geometries. (A–E) The representative stress-strain curves for the compressive measurements; (F) The Compressive strength and elastic modulus of the porous samples. Data are expressed as the mean ± SD.

pore walls were compressed. However, the Diamond and Gyroid scaffolds experienced a rapid increase in stress (region S1′; accompanied by an ~2%–6% train), and then yield terraces appeared in the curves (region S2′) for the samples, corresponding to the yield strength after elastic deformation. Finally, as the pore walls became increasingly broken, or densified (region S3′), the stress decreased. On the other hand, the stress-strain response of IWP scaffolds was consistent with the Diamond scaffolds, even if the former had lower peak stress before breakage. As shown in Fig. 3F, varying pore geometries of bioceramic scaffolds led to different compressive strengths and elastic moduli. The s-Diamond scaffolds showed the highest compressive strength of 54.73 ± 6.77 MPa and an elastic modulus of 436.87 ± 55.15 MPa. The s-Gyroid scaffolds showed a compressive strength of 50.27 ± 4.44 MPa and an elastic modulus of 404.56 ± 76.66 MPa. Interestingly, the sheet-type pore (s-Diamond and s-Gyroid) scaffolds displayed 3- to 4-fold higher strengths than their Diamond- or Gyroid-pore counterparts (15.97 ± 0.65 MPa and 12.46 ± 1.23 MPa), but their elastic moduli were similar to each other. Furthermore, the IWP scaffolds had a higher elastic modulus (591.37 ± 26.57 MPa) and a lower strength (9.83 ± 1.46 MPa) than the other scaffolds.

Fig. 4A–C illustrates the biodissolution (ion release and mass decrease) of porous scaffolds soaked in Tris-HCl buffer over two weeks. The s-Diamond and s-Gyroid scaffolds showed much faster magnesium ion release (~3.2–3.6 ppm in final) than the Diamond and Gyroid scaffold groups (~2.2–2.3 ppm in final). Among these different pore architectures, the sheet-type pore geometry could produce higher magnesium ion concentrations (~1.3–1.5-fold) at each time, which could be ascribed to the higher surface-to-volume ratio of sheet-type pore architectures (see Table 1). Note that the IWP scaffolds (low surface-to-volume ratio) also showed an appreciable magnesium ion release throughout the immersion stage (3.3 ppm in final). Fig. 4D shows the mass decrease of the porous scaffolds in Tris-HCl buffer over the course of 8 weeks. The diamond and gyroid architectures showed higher mass loss (~6%) within the initial 4 weeks than the sheet-type pore

architectures (~1.9%–2.3%), while the IWP scaffolds exhibited slower biodissolution and mass decrease (~0.9%). Finally, the scaffolds for these different pore geometries showed a 6.5%–8.7% mass decrease after 8 weeks. In addition, Fig. 4E–H illustrates the ion release of porous scaffolds soaked in SBF over two weeks. Similar release rates of calcium, silicon, and magnesium ions were shown from five scaffolds within the first week. Interestingly, the silicon ion concentration appeared to keep stable within the first week (Fig. 4F), which was similar to that in Tris-HCl buffer (Fig. 4B). Moreover, the calcium ion release in SBF was slower than that in Tris-HCl buffer, and the phosphorus ion concentration was decreased rapidly during the first week, implying that phosphate groups were consumed during this immersion process and the hydroxyapatite mineralization would occur fast on the pore wall of bioceramic scaffolds.

3.4. Proliferation and osteogenic differentiation of BMSCs on scaffolds

Cell proliferation and osteogenic differentiation on the pore wall of bioceramic scaffolds is an important biological function. The proliferation capacity of BMSCs on scaffolds was analyzed using CCK8 testing. Compared with cells incubated in the medium, BMSCs on the five groups of scaffolds showed a significant trend of enhanced proliferation. There was no significant difference between the groups (Fig. 5A). Both Western blot and RT-PCR analysis showed that the presence of bioceramic scaffolds significantly increased the expression of osteogenic genes (OPN and Runx-2) (Fig. 5B) and proteins (OPN and Runx-2) in BMSCs (Fig. 5C). The expression levels of osteoblast-related proteins and genes in cells incubated in Diamond and Gyroid scaffolds were significantly higher than those in the other groups. Live/dead cell staining showed that most of the cells attached to the scaffold were alive (Fig. 5D). BMSCs cultured with five kinds of scaffolds were evaluated using confocal microscopy observation (Fig. 5E). It was clear that the cells could effectively adhere to the pore walls. High levels of OPN expression are associated with late osteogenesis and bone matrix deposition. It was
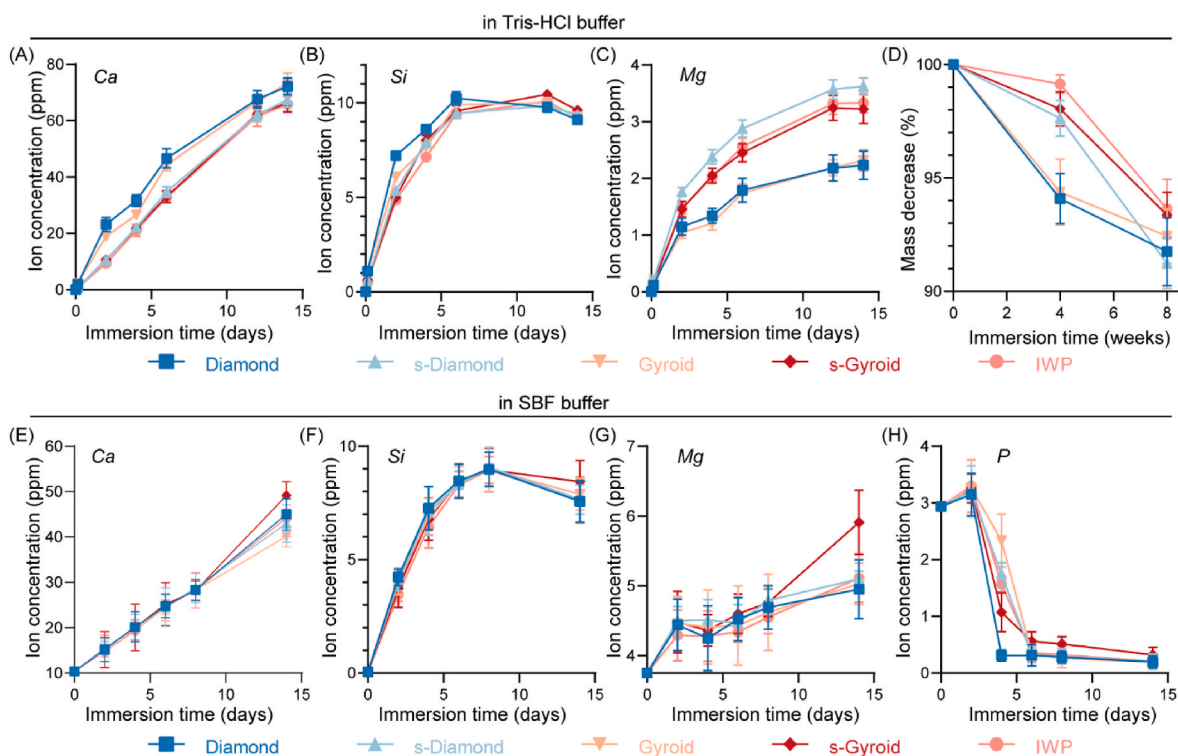

Fig. 4. *In vitro* biodegradation test of the CSi–Mg6 scaffolds in Tris-HCl and SBF buffers for different time stages. (A–C) The ion release (diluting tenfold) of Ca, Mg, and Si in Tris-HCl buffer for two weeks; (D) Mass decrease of the scaffold samples during immersion in Tris-HCl buffer for 4 and 8 weeks. (E–H) Changes in Ca, Si, Mg, and P ion concentrations (diluting tenfold) in SBF buffer for two weeks. Data are expressed as the mean ± SD.
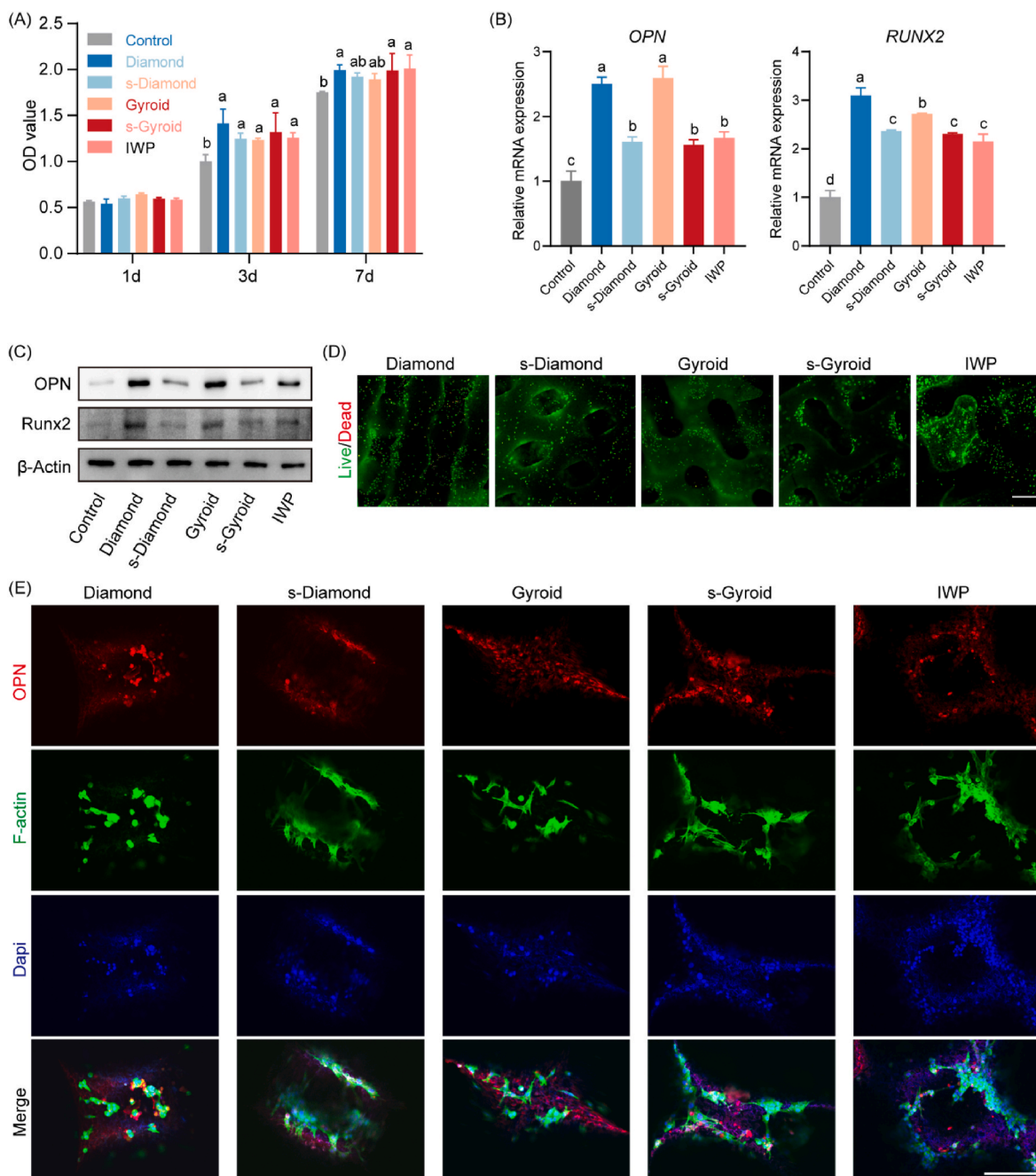
Fig. 5. (A) The viability of BMSCs cultured on different scaffolds after 1, 3, and 7 days measured by CCK-8. (B) Relative mRNA expression levels (normalized to β-actin) of osteogenesis-related genes (OPN and Runx-2) in BMSCs following a 7-day osteogenic incubation on different scaffolds. (C) Expression of osteogenic proteins (OPN and Runx-2) in BMSCs following a 7-day osteogenic incubation on different scaffolds. (D) Fluorescence staining of osteoclast progenitors (live/dead) grown on different scaffolds; viable cells were stained with calcein-AM (green fluorescence), while dead cells were stained with PI (red fluorescence). Scale bar = 500 μm. (E) Immunofluorescence staining of OPN of BMSCs seeded on different scaffolds after 7 d of incubation, scale bar = 200 μm. All data are expressed as the mean ± SD. Different letters represent significant differences between groups at the same time point, n = 3, $p < 0.05$.

confirmed that the CSi–Mg6 bioceramic scaffolds readily promote the high expression of OPN.

3.5. Initial evaluation of models for femoral bone defects

None of the rabbits displayed symptoms of infection, and they all survived long enough until the different time points for specimen harvesting (3–10 weeks). There was a mild inflammatory response during the early three weeks of post-treatment. The gross examination of the femur specimens at 10 weeks (Fig. S3A) revealed that all of the defects had healed, and no necrosis was evident in any of the femoral bone

specimens. Radiographic analysis of the X-ray image was utilized to assess the overall defect evolution and scaffold resorption (Fig. S3B). All porous implants demonstrated significant biodegradation over time, and the scaffolds showed significant resorption after 10 weeks.

3.6. μCT reconstruction and quantitative analysis

As shown in Figs. 6 and 7, the 2D/3D μCT-reconstructed images visually demonstrated the ingrowth of bone tissue from the sidewall pores of the scaffolds at 3–10 weeks post-surgery. Each scaffold showed different osteoconductive efficiencies, depending on the pore geometry,
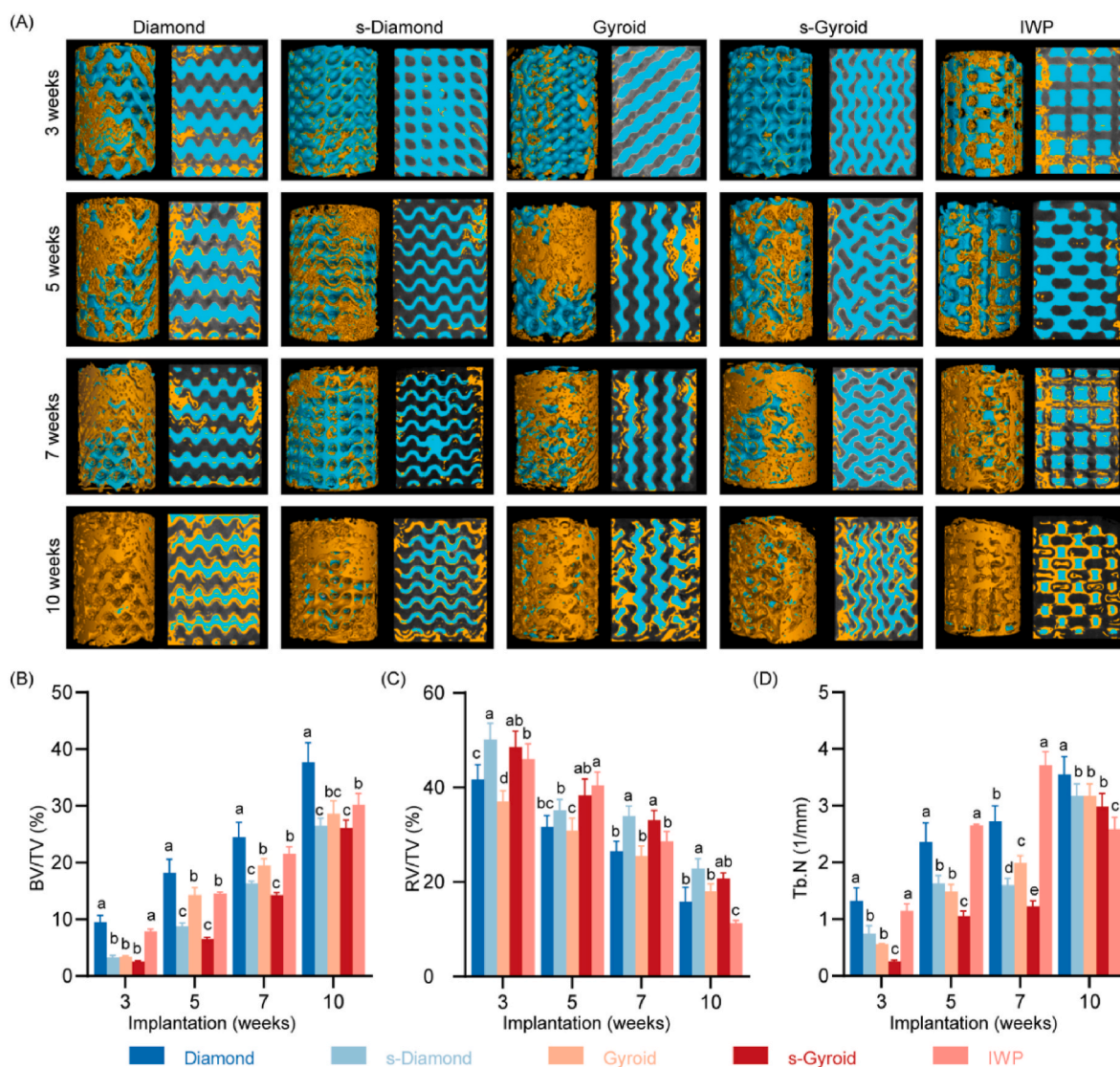
Fig. 6. (A) μCT reconstruction and cross-section images of the femoral bone defect implanted with scaffolds at 3−10 weeks after implantation. Blue: biomaterial; Yellow: neo-bone tissue. Quantitative data of BV/TV (B), RV/TV (C), and Tb. N (D) in the femoral bone defect implanted with the bioceramic scaffolds. Data are expressed as the mean ± SD. Different letters represent significant differences between groups at the same time point, n = 3, $p < 0.05$.

within 10 weeks. Moreover, an analysis of 3D μCT morphometry was conducted to quantify and characterize new bone formation. Some quantitative parameters, including the BV/TV, RV/TV, and Tb·N values represented the amounts of new bone tissue formed and material residual left in the bone defects (Fig. 6B–D). The Diamond and IWP scaffold groups gradually grew new bone tissue into their porous networks after 3 weeks (9.48 ± 1.17% and 7.97 ± 0.28% of BV/TV, respectively), while the Gyroid groups grew only some new bone tissue (~3.34 ± 0.18% of BV/TV). However, there was little new bone tissue in the sheet-type pore scaffolds. The s-Diamond and s-Gyroid scaffold groups showed very limited new bone tissue over a period of 10 weeks, while the Diamond and Gyroid scaffold groups showed adequate new bone tissue, and the porous architecture remained stable. The bone volume fractions for the Diamond and Gyroid scaffold groups were 37.64 ± 3.43% and 28.52 ± 2.28%, respectively, as shown in Fig. 6B. Importantly, the porous architectures in the Diamond and IWP scaffolds were filled by new bone tissue after 7 weeks (Fig. 6A and B). The 2D/3D images showed complete infiltration of the bioceramic scaffolds (blue) with new bone tissue (yellow), which led to the bridging of the defects in the porous architectures, in contrast to the incomplete bridging in the sheet-type pore architectures. The s-Diamond and s-Gyroid scaffold groups showed

significantly lower BV/TV and Tb·N values in the early stages (3–7 weeks; $p < 0.05$). Interestingly, the IWP group showed a decreased BV/TV value from 7 to 10 weeks, suggesting that the newly formed bone tissue would be remodeled before full maturation. Moreover, the sheet-type scaffold groups displayed a slower decline in RV/TV values throughout the course of implantation. This phenomenon is possibly attributed to the low initial porosity and new bone ingrowth. Furthermore, the CSi–Mg6 bioceramic scaffolds maintained their pore wall structures throughout the entire experiment without any collapse or structural cracks, indicating a high level of structural stability *in vivo* under such stress-induced conditions.

Importantly, 3D reconstruction of the new bone tissue in the region of interest (ROI, 5 mm × 5 mm × 2 mm) of the scaffold was performed (Fig. 7A) in order to observe the bone regeneration in the early stage, and the parameters such as BV/TV, Tb·N, Tb·Th were analyzed (Fig. 7B–D). The Diamond and IWP group both showed significantly higher BV/TV, Tb·N, and Tb·Th values than the other groups at 7 weeks.

3.7. Histological analysis

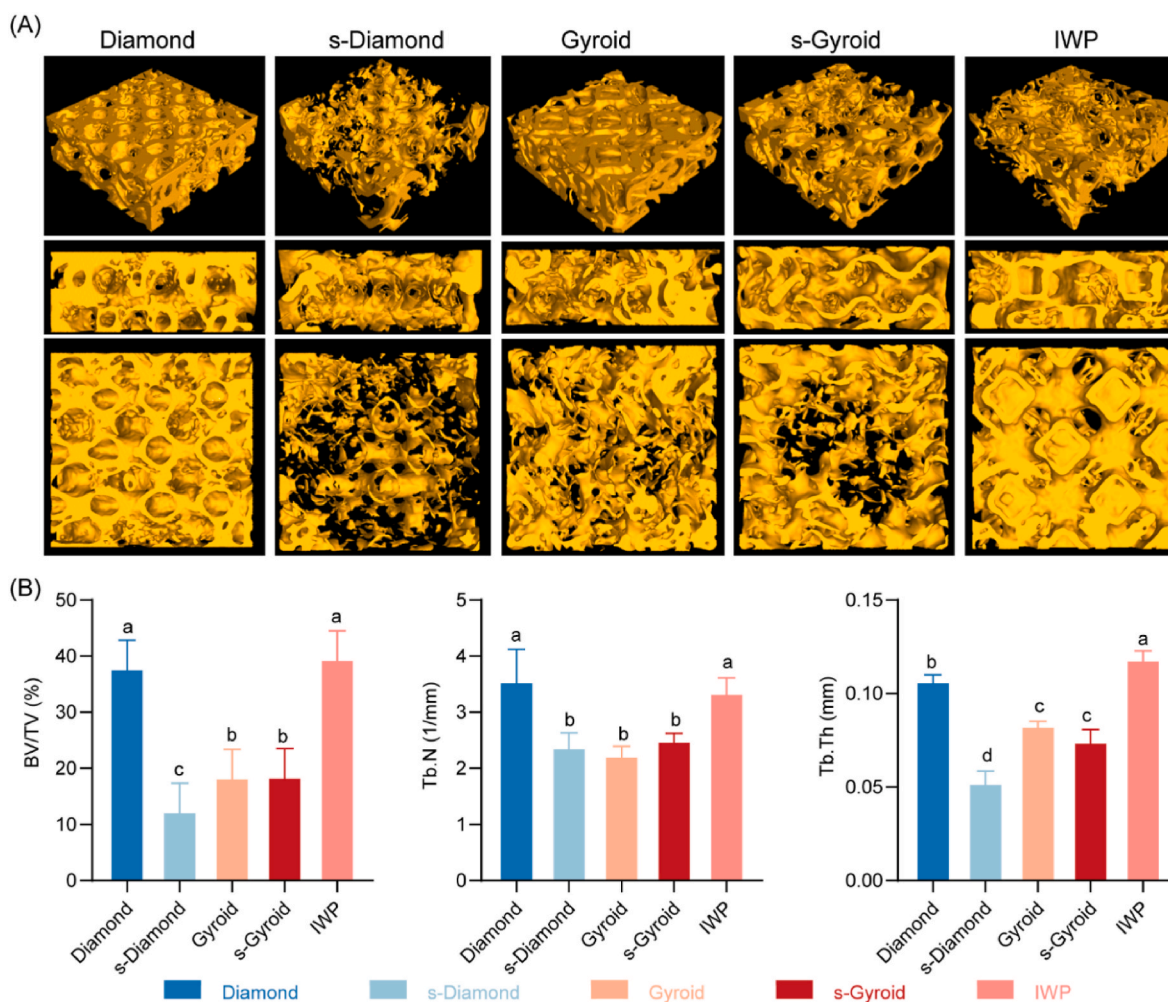Histological analysis was performed to demonstrate the dynamic

Fig. 7. (A) 3D reconstructed images of femoral new bone formation in the region of interest (ROI, 5 mm × 5 mm × 2 mm) of the bioceramic scaffolds after 7 weeks by μCT. (B) Quantitative data of BV/TV, Tb. N, and Tb·Th in the regions of interest. Data are expressed as the mean ± SD. Different letters represent significant differences between groups at the same time point, n = 3, $p < 0.05$.

process of new bone tissue ingrowth in the five groups of scaffolds. The HE staining images (Fig. 8A) showed that the new bone tissue regenerated preferentially into the outermost porous networks of all scaffold groups within 3 weeks, which was similar to the 2D μCT reconstructed images, as shown in Fig. 6. After 5 weeks, new bone ingrowth could be observed from the peripheral region to the internal region of all porous architectures. Moreover, the bioceramic frameworks were observed clearly in the bone defects after 5 weeks, and the pore morphology could be easily distinguished among the five groups of scaffolds.

McNeal staining histological sections of the bone specimens from 3 to 10 weeks are displayed in Fig. 8B and C. Mineralized bone tissue was stained red, and unmineralized tissue was stained blue. The new bone tissue was dark red, while the mature bone tissue was light. None of the groups experienced any obvious reactions to foreign bodies. The new bone tissue gradually gained access to the interior of the scaffolds as a result of the extensive macroporous networks of the scaffold. Among them, the IWP scaffold groups showed slower bone tissue ingrowth throughout the experiment, with a relative bone area of 6.52 ± 1.23%. Comparatively speaking, the other four scaffold groups showed appreciable new bone growth in the early stages after implantation (3–5 weeks). However, only the Diamond and Gyroid scaffolds maintained a faster growth rate in the later stages (7–10 weeks) and were gradually filled with new bone tissue. Finally, the Diamond and Gyroid scaffolds showed the most objective bone tissue area fraction at 16.90 ± 0.58% and 17.49 ± 1.48%, respectively (Fig. 8D). For the sheet-type pore

architectures, it was seen from the unit observed under high magnification (Fig. 8C) that there was a deposit of osteoid collagens at the tissue–material interface in the early stages (5 weeks), whereas the newly formed bone tissue was already generated in the macropores of the sheet-free scaffold groups. Many mature bones have developed in these scaffolds.

4. Discussion

The ideal scaffolds should have structural durability, bioactivity, and continuous curvature, and they should be permeable at the pore surface to facilitate the nutrient transport and migration of osteogenic cells [45]. It is crucial to clarify the mechanical and biological properties of bioceramic scaffolds with curvature pore surfaces (i.e., TPMS pore architectures) and pore geometries. Pore geometry approaches have been developed, and their effects have been investigated to explore the influences of pore geometry on bone regeneration capacity *in situ* at the early stage.

Ca-silicate bioceramics are highly bioactive inorganic materials that have been studied in tissue engineering, bioactive aids, and even ion therapy [46–49]. Many strategies have been used for the preparation and modification of these bioceramics, and porous scaffolds are by far the most studied application. In this study, we printed nonstoichiometric wollastonite scaffolds ($Ca_{0.94}Mg_{0.06}SiO_3$) with exceptional bioactivity, biodegradability, and osteoconductivity [50–52]. The DLP-based
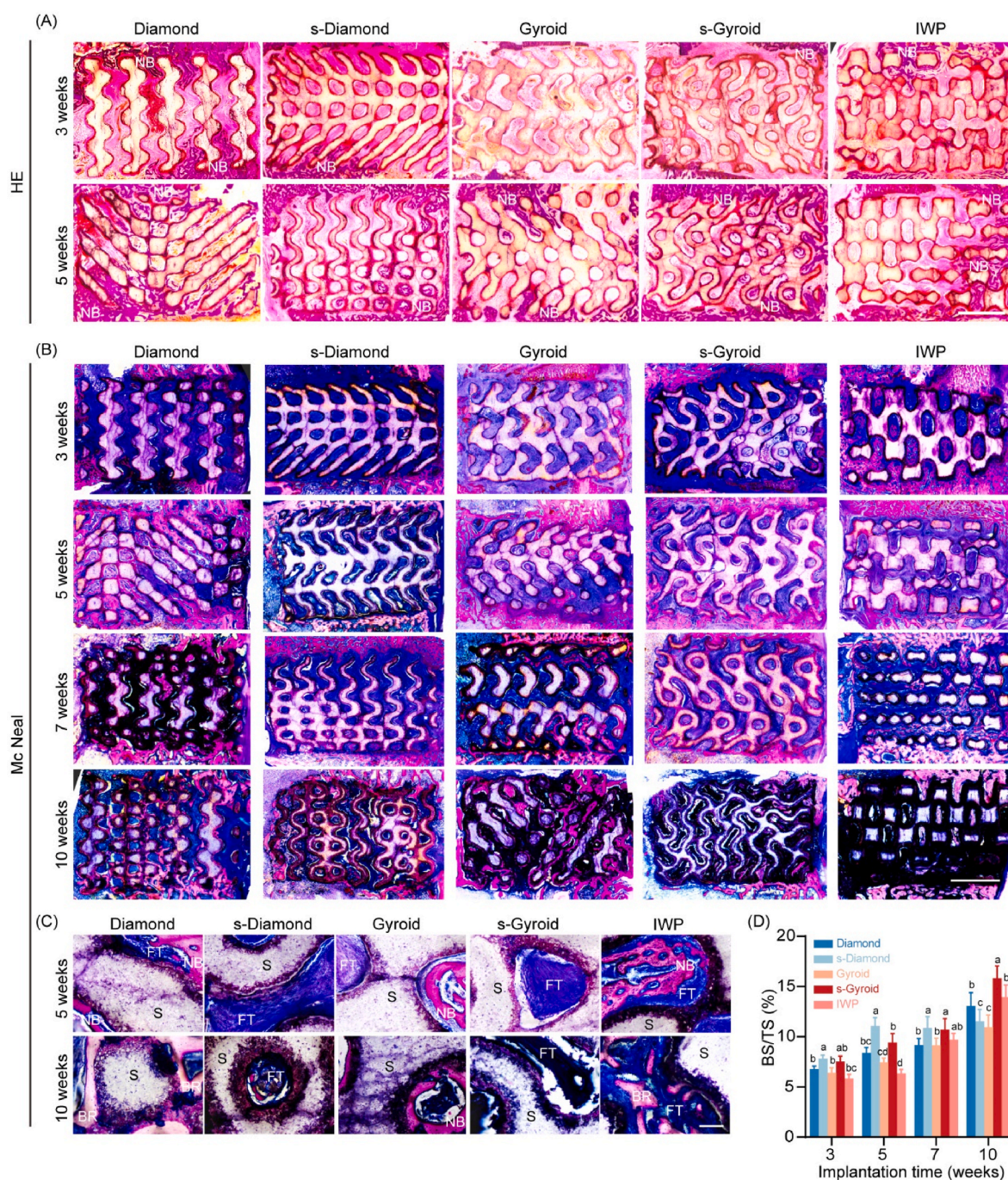
Fig. 8. (A) HE straining images of the femoral bone defects implanted with bioceramic scaffolds. NB: newly formed bone tissue. NB: newly formed bone tissue. Scale bar = 2 mm. (B) Overviews of the representative histological sections (McNeal staining) of the bioceramic scaffolds at 3−10 weeks after implantation. Scale bar = 2 mm. (C) The 100-fold magnifications (McNeal staining) of the inner regions of the scaffolds in the femoral defects at 5 and 10 weeks after implantation, respectively. S: scaffolds; FT: fibrous tissue; NB: newly formed bone tissue; BR: bone remodeling regions. Scale bar = 500 μm. (D) Quantitative data of BS/TS in Mc Neal staining images of the femoral bone defects implanted with bioceramic scaffolds. Data are expressed as the mean ± SD. Different letters represent significant differences between groups at the same time point, n = 3, $p < 0.05$.

printing process is versatile for a variety of bioceramic compositions [53]. The optimal pore size and porosity of bioceramic scaffolds are designed to be greater than 500 μm and 50%, respectively, to provide good permeability [52,54,55]. The pore network model of the scaffold was obtained based on the principle of maximum sphere algorithm. Parameters such as pore diameter and pore distribution can be obtained by the ball-and-stick model. It allowed us to minimize differences in bone regeneration efficiency caused by scaffold pore size.

In general, the biodegradable characteristics and ion release

behavior are both important factors for initiating osteogenesis in macroporous bioceramics [56,57]. Pure CSi bioceramics have been demonstrated to have good bioactivity due to their rapid biodissolution rates and HA mineralization potentials *in vitro*. However, pure CSi scaffolds show low structural stability in bone defects due to their rapid biodegradation *in vivo* [46]. It is abnormal but expected that the CSi–Mg6 scaffolds with five types of TPMS pore topologies show a slight difference in bio-dissolution and ion release *in vitro* (Fig. 4). We found that a dilute Mg substitution could improve the sintering properties of

wollastonite bioceramics in our previous studies, and the substitution may enhance the densification of the pore wall, which is considered favorable for inhibiting ceramic biodegradation [40]. Thus, enhancing the structural stability of such scaffolds is beneficial for studying the effect of pore geometry on new bone ingrowth efficacy. In addition, we prepared the CSi–Mg6 scaffolds with a significant compressive strength (>10 MPa) while ensuring their high porosity (>50%) and large average pore size (>500 μm) in a previous study [29]. These properties demonstrate that replicating 3D models and producing scaffolds with a wide variety of pore geometries can be easily achieved through a fabrication process based on our findings. To ensure the structural stability of scaffolds during new bone ingrowth, the mechanical properties of porous implants are often dependent on porosity and pore size.

Interestingly, the CSi–Mg6 bioceramic scaffolds display significantly different compressive strengths (<20 MPa or >50 MPa) because of slight variations in the pore wall structure and pore size distribution in each unit cell. Additionally, the stress-strain diagrams exhibit a similar trend to those of typical brittle bioceramics, but the porous scaffolds with and without sheet-type structures show subtle differences in elastic responses. Two factors may contribute to the mechanical properties of the CSi–Mg6 scaffolds: the slightly lower porosity of the sheet-type pore architectures (Table 1), which may contribute to the enhancement of compressive resistance, and the higher supporting pore wall density of sheet-type unit cells, which help to increase the construct collapse resistance. On the basis of macro/microscopic observations (Fig. 2), this study demonstrates that DLP-based 3D printing is capable of reproducing the intricate microstructures of 3D models with precisely tuned interior architecture and connectivity. There is a well-developed set of interconnected pores in all scaffolds, and importantly, the dimensions of the interconnected pores are maintained as they are in the CAD model throughout the study, which aids in tracking the regenerative progress as a function of pore geometry over time. In particular, the sheet-type pore architecture is extremely favorable for enhancing the compressive resistance of the scaffolds. It can be concluded that the curved surface-based pore wall structure exhibits excellent flexibility in tailoring mechanical properties.

As shown in Fig. 6, the CSi–Mg6 scaffolds with different pore architectures possess appreciable structural stability throughout the implantation stage (3–10 weeks) but are followed by significantly different new bone tissue ingrowth behavior, which is advantageous for dynamic observations of the bone repair behavior in the five types of pore architectures over time. However, the early-stage new bone tissue ingrowth cannot be attributed to appreciable Ca, Si, or Mg release because the osteogenic capability is different in the Diamond, Gyroid, and IWP pore scaffolds. Generally, an increase in pore size is beneficial for cell activity, fibrous vascularization, and new bone ingrowth [4,58, 59]. Our previous studies have found that pore sizes >400 μm could enhance early-stage new bone formation [39]. Thus, in addition to the inherent physicochemical properties of the CSi–Mg6 bioceramics, the pore geometry plays a critical role in determining the osteogenic capabilities. In this study, we demonstrate a difference in the osteogenic differentiation of cells and amount of early-stage bone tissue ingrowth between scaffolds with and without sheet-type pore architectures, with the latter showing a significantly better ability to induce osteogenic differentiation (Fig. 5) and greater amount of bone tissue (Fig. 7). Although the scaffolds are all manufactured by using CSi–Mg6 bioceramic, there is a consistent difference in the osteogenic rate related to the pore geometry-driven osteogenic response. Additionally, once the appreciable new bone tissue transforms into porous scaffolds, much faster bone remodeling can occur in such pore architecture. This finding may be related to the higher surface area to volume ratio of sheet-type pore architectures compared to the other architectures.

According to the μCT reconstruction and histological analysis, faster bone growth rates are maintained throughout the process, and almost all defects are completely repaired by new bone tissue of a similar density to the surrounding bone in the Diamond and Gyroid scaffold groups

(Fig. 6−8). This finding implies that the porous network geometry of bioceramic scaffolds has a significant impact on osteoconduction. In contrast, only a small amount of bone formation is observed in the s-Diamond, s-Gyroid, and IWP scaffolds after 3 weeks and appreciable new bone tissue ingrowth after 7 weeks (Fig. 7). These scaffolds present a lower degree of new bone tissue accumulation, although all pores are interconnected well and all dimensions, curvature, and geometry are compatible with the trabecular bone mineral network [4,19]. Moreover, it is worth noting that although the pore size and porosity are similar between the scaffolds with and without sheet-type pore architecture, the sheet-type pore geometries show thinner wall thickness but more pore wall volume in unit cell (Fig. S4), and thus may undergo higher resistance before structural collapse (higher compressive strength) under compression condition. Meanwhile, it is reasonable to consider that these two types of different pore structural characteristics may contribute the different osteogenic cell migration, fibrovascularization and new bone ingrowth in the early stage.

In general, the conventional biomimetic designs of porous scaffolds are mainly focused on two aspects: microstructural and compositional similarity to the native bone. However, biomimetic porous biomaterials, such as Ca-phosphate-based (hybrid) scaffolds [60,61], cannot resolve clinical challenges due to the suboptimal bioactive response and junior structural support of such man-made composite systems *in vivo*. Moreover, the 3D-printed synthetic HA scaffolds mimicking the trabecular architectures (i.e., curve surface pore) of native bone only replicate the interconnected macropore architectures but do not provide any osteostimulative activity [19]. The rationale behind the selection of porous biomaterials extends beyond merely altering their pore architectures (pore size, pore interconnection) to the arrangement of pore size distributions and curvatures that could be tailored to influence internal structural stability and bioactive ion release, which can facilitate bone regeneration. According to these studies, the pore architectures of the bioactive ceramic scaffolds manufactured by DLP are important in challenging bone defects where unsatisfactory bone repair (e.g., delayed union or nonunion) cannot be attributed to only the physicochemical properties of the artificial implants. Considering these concerns, future studies should concentrate on the role of nonstructural defined pore topologies in Ca-silicate scaffolds in bone regeneration, especially in translational medical studies involving porous bioceramics.

5. Conclusion

In summary, a series of porous Ca-silicate bioceramic scaffolds with precise pore geometries were fabricated in this study for bone regeneration and repair *in situ*. The sheet-type pore geometries exhibited notable compressive strength and a faster release rate of Mg *in vitro*. However, the sheet-type pore geometries did not show rapid bone tissue formation in the critical-sized bone defects in the early stage because of the above phenomena. In contrast, the Diamond and IWP pore geometries were beneficial for osteoconduction. As a result of these experiments, we demonstrated that precisely tuned pore geometries of TPMS-based bioceramic scaffolds exhibited excellent bone growth responses at an early development stage. These new findings suggest that the design of pore morphology and structure cannot be limited to mimicking the trabecular architecture of cancellous bone; instead, pore geometry also needs to be optimized to promote the ingrowth of new bone tissue in the early stage.

Ethics approval and consent to participate

All experimental protocols were approved by the Animal Care and Use Committee of Zhejiang University. All animals received humane care according to the criteria outlined in the "Guide for the Care and Use of Laboratory Animals".

CRediT authorship contribution statement

Miaoda Shen: Formal analysis, Data curation, Writing – original draft. **Yifan Li:** Validation, Investigation, Writing – original draft. **Fengling Lu:** Formal analysis, Data curation. **Yahui Gou:** Investigation. **Cheng Zhong:** Validation. **Shukun He:** Investigation. **Chenchen Zhao:** Validation. **Guojing Yang:** Resources. **Lei Zhang:** Supervision. **Xianyan Yang:** Writing – review & editing, Supervision, Project administration. **Zhongru Gou:** Writing – review & editing, Supervision. **Sanzhong Xu:** Writing – review & editing.

Declaration of competing interest

The authors declare that they have no conflicts of interest.

Acknowledgments

Appendix A. Supplementary data

Supplementary data to this article can be found online at https://doi.org/10.1016/j.bioactmat.2023.02.012.

References

[1] A.A. Zadpoor, Bone tissue regeneration: the role of scaffold geometry, Biomater. Sci. 3 (2015) 231–245, https://doi.org/10.1039/C4BM00291A.

[2] A. Gleadall, D. Visscher, J. Yang, D. Thomas, J. Segal, Review of additive manufactured tissue engineering scaffolds: relationship between geometry and performance, Burns & Trauma 6 (2018), https://doi.org/10.1186/s41038-018-0121-4.

[3] A. Marques, G. Miranda, F. Silva, P. Pinto, Ó. Carvalho, Review on current limits and potentialities of technologies for biomedical ceramic scaffolds production, J. Biomed. Mater. Res. 109 (2021) 377–393, https://doi.org/10.1002/jbm.b.34706.

[4] D. Barba, E. Alabort, R.C. Reed, Synthetic bone: design by additive manufacturing, Acta Biomater. 97 (2019) 637–656, https://doi.org/10.1016/j.actbio.2019.07.049.

[5] A.C. Jones, C.H. Arns, D.W. Hutmacher, B.K. Milthorpe, A.P. Sheppard, M.A. Knackstedt, The correlation of pore morphology, interconnectivity and physical properties of 3D ceramic scaffolds with bone ingrowth, Biomaterials 30 (2009) 1440–1451, https://doi.org/10.1016/j.biomaterials.2008.10.056.

[6] M.-T. Hsieh, M.R. Begley, L. Valdevit, Architected implant designs for long bones: advantages of minimal surface-based topologies, Mater. Des. 207 (2021), 109838, https://doi.org/10.1016/j.matdes.2021.109838.

[7] D. He, H. Li, Biomaterials affect cell-cell interactions in vitro in tissue engineering, J. Mater. Sci. Technol. 63 (2021) 62–72, https://doi.org/10.1016/j.jmst.2020.03.022.

[8] S.-W. Choi, Y. Zhang, M.R. MacEwan, Y. Xia, Neovascularization in biodegradable inverse opal scaffolds with uniform and precisely controlled pore sizes, Advanced Healthcare Materials 2 (2013) 145–154, https://doi.org/10.1002/adhm.201200106.

[9] V. Karageorgiou, D. Kaplan, Porosity of 3D biomaterial scaffolds and osteogenesis, Biomaterials 26 (2005) 5474–5491, https://doi.org/10.1016/j.biomaterials.2005.02.002.

[10] F. Bai, Z. Wang, J. Lu, J. Liu, G. Chen, R. Lv, J. Wang, K. Lin, J. Zhang, X. Huang, The correlation between the internal structure and vascularization of controllable porous bioceramic materials in vivo: a quantitative study, Tissue Eng. 16 (2010) 3791–3803, https://doi.org/10.1089/ten.tea.2010.0148.

[11] M. Descamps, T. Duhoo, F. Monchau, J. Lu, P. Hardouin, J.C. Hornez, A. Leriche, Manufacture of macroporous β-tricalcium phosphate bioceramics, J. Eur. Ceram. Soc. 28 (2008) 149–157, https://doi.org/10.1016/j.jeurceramsoc.2007.05.025.

[12] S. Deville, E. Saiz, A.P. Tomsia, Freeze casting of hydroxyapatite scaffolds for bone tissue engineering, Biomaterials 27 (2006) 5480–5489, https://doi.org/10.1016/j.biomaterials.2006.06.028.

[13] S. Gómez, M.D. Vlad, J. López, E. Fernández, Design and properties of 3D scaffolds for bone tissue engineering, Acta Biomater. 42 (2016) 341–350, https://doi.org/10.1016/j.actbio.2016.06.032.

[14] C. Xu, H. Liu, H. Yang, L. Yang, A green biocompatible fabrication of highly porous functional ceramics with high strength and controllable pore structures, J. Mater. Sci. Technol. 32 (2016) 729–732, https://doi.org/10.1016/j.jmst.2016.07.002.

[15] J. Zhang, C. Zhao, R. Sheng, K. Lin, X. Wang, S. Zhang, Construction of a hierarchical micro-/submicro-/nanostructured 3D-printed Ti6Al4V surface feature to promote osteogenesis: involvement of Sema7A through the ITGB1/FAK/ERK signaling pathway, ACS Appl. Mater. Interfaces 14 (2022) 30571–30581, https://doi.org/10.1021/acsami.2c06454.

[16] C. Yin, T. Zhang, Q. Wei, H. Cai, Y. Cheng, Y. Tian, H. Leng, C. Wang, S. Feng, Z. Liu, Surface treatment of 3D printed porous Ti6Al4V implants by ultraviolet photofunctionalization for improved osseointegration, Bioact. Mater. 7 (2022) 26–38, https://doi.org/10.1016/j.bioactmat.2021.05.043.

[17] E. Babaie, S.B. Bhaduri, Fabrication aspects of porous biomaterials in orthopedic applications: a review, ACS Biomater. Sci. Eng. 4 (2018) 1–39, https://doi.org/10.1021/acsbiomaterials.7b00615.

[18] A. Bigham, F. Foroughi, E. Rezvani Ghomi, M. Rafienia, R.E. Neisiany, S. Ramakrishna, The journey of multifunctional bone scaffolds fabricated from traditional toward modern techniques, Bio-Des. Manuf. 3 (2020) 281–306, https://doi.org/10.1007/s42242-020-00094-4.

[19] F. Baino, G. Magnaterra, E. Fiume, A. Schiavi, L. Tofan, M. Schwentenwein, E. Verné, Digital light processing stereolithography of hydroxyapatite scaffolds with bone-like architecture, permeability, and mechanical properties, J. Am. Ceram. Soc. 105 (2022) 1648–1657, https://doi.org/10.1111/jace.17843.

[20] F. Tavangarian, A. Fahami, G. Li, M. Kazemi, A. Forghani, Structural characterization and strengthening mechanism of forsterite nanostructured scaffolds synthesized by multistep sintering method, J. Mater. Sci. Technol. 34 (2018) 2263–2270, https://doi.org/10.1016/j.jmst.2018.06.010.

[21] S.J. Hollister, Porous scaffold design for tissue engineering, Nat. Mater. 4 (2005) 518–524, https://doi.org/10.1038/nmat1421.

[22] A. Zhang, H. Chen, Y. Liu, N. Wu, B. Chen, X. Zhao, Q. Han, J. Wang, Customized reconstructive prosthesis design based on topological optimization to treat severe proximal tibia defect, Bio-Des. Manuf. 4 (2021) 87–99, https://doi.org/10.1007/s42242-020-00102-7.

[23] E. Peng, D. Zhang, J. Ding, Ceramic robocasting: recent achievements, potential, and future developments, Adv. Mater. 30 (2018), 1802404, https://doi.org/10.1002/adma.201802404.

[24] T. Distler, N. Fournier, A. Grünewald, C. Polley, H. Seitz, R. Detsch, A.R. Boccaccini, Polymer-bioactive glass composite filaments for 3D scaffold manufacturing by fused deposition modeling: fabrication and characterization, Front. Bioeng. Biotechnol. 8 (2020) 552, https://doi.org/10.3389/fbioe.2020.00552.

[25] I. Zein, D.W. Hutmacher, K.C. Tan, S.H. Teoh, Fused deposition modeling of novel scaffold architectures for tissue engineering applications, Biomaterials 23 (2002) 1169–1185, https://doi.org/10.1016/S0142-9612(01)00232-0.

[26] S.-I. Roohani-Esfahani, P. Newman, H. Zreiqat, Design and fabrication of 3D printed scaffolds with a mechanical strength comparable to cortical bone to repair large bone defects, Sci. Rep. 6 (2016), https://doi.org/10.1038/srep19468.

[27] D.W. Johnson, C. Sherborne, M.P. Didsbury, C. Pateman, N.R. Cameron, F. Claeyssens, Macrostructuring of emulsion-templated porous polymers by 3D laser patterning, Adv. Mater. 25 (2013) 3178–3181, https://doi.org/10.1002/adma.201300552.

[28] L. Le Guéhennec, D. Van hede, E. Plougonven, G. Nolens, B. Verlée, M. De Pauw, F. Lambert, Vitro and in vivo biocompatibility of calcium-phosphate scaffolds three-dimensional printed by stereolithography for bone regeneration, J. Biomed. Mater. Res. 108 (2020) 412–425, https://doi.org/10.1002/jbm.a.36823.

[29] F. Lu, R. Wu, M. Shen, L. Xie, M. Liu, Y. Li, S. Xu, L. Wan, X. Yang, C. Gao, Z. Gou, Rational design of bioceramic scaffolds with tuning pore geometry by stereolithography: microstructure evaluation and mechanical evolution, J. Eur. Ceram. Soc. 41 (2021) 1672–1682, doi: 10.1016/j.jeurceramsoc.2020.10.002.

[30] I. Uiiah, L. Cao, W. Cui, Q. Xu, R. Yang, K. Tang, X. Zhang, Stereolithography printing of bone scaffolds using biofunctional calcium phosphate nanoparticles, J. Mater. Sci. Technol. 88 (2021) 99–108, https://doi.org/10.1016/j.jmst.2021.01.062.

[31] B. Charbonnier, C. Laurent, G. Blanc, O. Valfort, D. Marchat, Porous bioceramics produced by impregnation of 3D-printed wax mold: ceramic architectural control and process limitations, Adv. Eng. Mater. 18 (2016) 1728–1737, https://doi.org/10.1002/adem.201600308.

[32] M. Zhang, R. Lin, X. Wang, J. Xue, C. Deng, C. Feng, H. Zhuang, J. Ma, C. Qin, L. Wan, J. Chang, C. Wu, 3D printing of Haversian bone–mimicking scaffolds for multicellular delivery in bone regeneration, Sci. Adv. 6 (2020) doi: 10.1126/sciadv.aaz6725.

[33] A.L. Mackay, Periodic minimal surfaces from finite element methods, Chem. Phys. Lett. 221 (1994) 317–321, https://doi.org/10.1016/0009-2614(94)00256-8.

[34] S.M. Giannitelli, D. Accoto, M. Trombetta, A. Rainer, Current trends in the design of scaffolds for computer-aided tissue engineering, Acta Biomater. 10 (2014) 580–594, https://doi.org/10.1016/j.actbio.2013.10.024.

[35] S.C. Kapfer, S.T. Hyde, K. Mecke, C.H. Arns, G.E. Schröder-Turk, Minimal surface scaffold designs for tissue engineering, Biomaterials 32 (2011) 6875–6882, https://doi.org/10.1016/j.biomaterials.2011.06.012.

[36] F.P.W. Melchels, K. Bertoldi, R. Gabbrielli, A.H. Velders, J. Feijen, D.W. Grijpma, Mathematically defined tissue engineering scaffold architectures prepared by stereolithography, Biomaterials 31 (2010) 6909–6916, https://doi.org/10.1016/j.biomaterials.2010.05.068.

[37] G. Yu, Z. Li, S. Li, Q. Zhang, Y. Hua, H. Liu, X. Zhao, D.T. Dhaidhai, W. Li, X. Wang, The select of internal architecture for porous Ti alloy scaffold: a compromise

between mechanical properties and permeability, Mater. Des. 192 (2020), 108754, https://doi.org/10.1016/j.matdes.2020.108754.

[38] F.S.L. Bobbert, K. Lietaert, A.A. Eftekhari, B. Pouran, S.M. Ahmadi, H. Weinans, A. A. Zadpoor, Additively manufactured metallic porous biomaterials based on minimal surfaces: a unique combination of topological, mechanical, and mass transport properties, Acta Biomater. 53 (2017) 572–584, https://doi.org/10.1016/j.actbio.2017.02.024.

[39] S.-Y. Park, K.-S. Kim, B. AlMangour, D. Grzesiak, K.-A. Lee, Effect of unit cell topology on the tensile loading responses of additive manufactured CoCrMo triply periodic minimal surface sheet lattices, Mater. Des. 206 (2021), 109778, https://doi.org/10.1016/j.matdes.2021.109778.

[40] J. Xie, X. Yang, H. Shao, J. Ye, Y. He, J. Fu, C. Gao, Z. Gou, Simultaneous mechanical property and biodegradation improvement of wollastonite bioceramic through magnesium dilute doping, J. Mech. Behav. Biomed. Mater. 54 (2016) 60–71, doi: 10.1016/j.jmbbm.2015.09.012.

[41] H. Shao, Y. He, J. Fu, D. He, X. Yang, J. Xie, C. Yao, J. Ye, S. Xu, Z. Gou, 3D printing magnesium-doped wollastonite/β-TCP bioceramics scaffolds with high strength and adjustable degradation, J. Eur. Ceram. Soc. 36 (2016) 1495–1503, https://doi.org/10.1016/j.jeurceramsoc.2016.01.010.

[42] Z. Cai, Z. Liu, X. Hu, H. Kuang, J. Zhai, The effect of porosity on the mechanical properties of 3D-printed triply periodic minimal surface (TPMS) bioscaffold, Bio-Des. Manuf. 2 (2019) 242–255, https://doi.org/10.1007/s42242-019-00054-7.

[43] M. Wohlgemuth, N. Yufa, J. Hoffman, E.L. Thomas, Triply periodic bicontinuous cubic microdomain morphologies by symmetries, Macromolecules 34 (2001) 6083–6089, https://doi.org/10.1021/ma0019499.

[44] C. Kilkenny, W. Browne, I.C. Cuthill, M. Emerson, D.G. Altman, Animal research: Reporting in vivo experiments: the ARRIVE guidelines, Br. J. Pharmacol. 160 (2010) 1577–1579, https://doi.org/10.1111/j.1476-5381.2010.00872.x.

[45] H. Wei, J. Cui, K. Lin, J. Xie, X. Wang, Recent advances in smart stimuli-responsive biomaterials for bone therapeutics and regeneration, Bone Res 10 (2022) 17, https://doi.org/10.1038/s41413-021-00180-y.

[46] S. Xu, K. Lin, Z. Wang, J. Chang, L. Wang, J. Lu, C. Ning, Reconstruction of calvarial defect of rabbits using porous calcium silicate bioactive ceramics, Biomaterials 29 (2008) 2588–2596, https://doi.org/10.1016/j.biomaterials.2008.03.013.

[47] S. Ni, K. Lin, J. Chang, L. Chou, β-CaSiO3/β-Ca3(PO4)2 composite materials for hard tissue repair:In vitro studies, J. Biomed. Mater. Res. 85A (2008) 72–82, https://doi.org/10.1002/jbm.a.31390.

[48] C. Wu, W. Fan, Y. Zhou, Y. Luo, M. Gelinsky, J. Chang, Y. Xiao, 3D-printing of highly uniform CaSiO3 ceramic scaffolds: preparation, characterization and in vivo osteogenesis, J. Mater. Chem. 22 (2012) 12288, https://doi.org/10.1039/c2jm30566f.

[49] T. Chen, Z. Zhang, D. Weng, L. Lu, X. Wang, M. Xing, H. Qiu, M. Zhao, L. Shen, Y. Zhou, J. Chang, H.-P. Li, Ion therapy of pulmonary fibrosis by inhalation of ionic solution derived from silicate bioceramics, Bioact. Mater. 6 (2021) 3194–3206, https://doi.org/10.1016/j.bioactmat.2021.02.013.

[50] A. Liu, M. Sun, H. Shao, X. Yang, C. Ma, D. He, Q. Gao, Y. Liu, S. Yan, S. Xu, Y. He, J. Fu, Z. Gou, The outstanding mechanical response and bone regeneration capacity of robocast dilute magnesium-doped wollastonite scaffolds in critical size bone defects, J. Mater. Chem. B. 4 (2016) 3945–3958, https://doi.org/10.1039/c6tb00449k.

[51] J. Wang, X. Dai, Y. Peng, M. Liu, F. Lu, X. Yang, Z. Gou, J. Ye, Digital light processing strength-strong ultra-thin bioceramic scaffolds for challengeable orbital bone regeneration and repair in Situ, Appl. Mater. Today 22 (2021), 100889, https://doi.org/10.1016/j.apmt.2020.100889.

[52] R. Wu, Y. Li, M. Shen, X. Yang, L. Zhang, X. Ke, G. Yang, C. Gao, Z. Gou, S. Xu, Bone tissue regeneration: the role of finely tuned pore architecture of bioactive scaffolds before clinical translation, Bioact. Mater. 6 (2021) 1242–1254, doi: 10.1016/j.bioactmat.2020.11.003.

[53] X. Shi, A. Nommeots-Nomm, N.M. Todd, A. Devlin-Mullin, H. Geng, P.D. Lee, C. A. Mitchell, J.R. Jones, Bioactive glass scaffold architectures regulate patterning of bone regeneration in vivo, Appl. Mater. Today 20 (2020) 100770, https://doi.org/10.1016/j.apmt.2020.100770.

[54] F. Wu, J. Yang, X. Ke, S. Ye, Z. Bao, X. Yang, C. Zhong, M. Shen, S. Xu, L. Zhang, Z. Gou, G. Yang, Integrating pore architectures to evaluate vascularization efficacy in silicate-based bioceramic scaffolds, Regenerative Biomaterials 9 (2022), https://doi.org/10.1093/rb/rbab077.

[55] S.A. Naghavi, M. Tamaddon, A. Marghoub, K. Wang, B.B. Babamiri, K. Hazeli, W. Xu, X. Lu, C. Sun, L. Wang, M. Moazen, L. Wang, D. Li, C. Liu, Mechanical characterisation and numerical modelling of TPMS-based gyroid and diamond Ti6Al4V scaffolds for bone implants: an integrated approach for translational consideration, Bioengineering 9 (2022) 504, https://doi.org/10.3390/bioengineering9100504.

[56] M. Diba, O.-M. Goudouri, F. Tapia, A.R. Boccaccini, Magnesium-containing bioactive polycrystalline silicate-based ceramics and glass-ceramics for biomedical applications, Curr. Opin. Solid State Mater. Sci. 18 (2014) 147–167, https://doi.org/10.1016/j.cossms.2014.02.004.

[57] M. Diba, F. Tapia, A.R. Boccaccini, L.A. Strobel, Magnesium-Containing bioactive glasses for biomedical applications, Int. J. Appl. Glass Sci. 3 (2012) 221–253, https://doi.org/10.1111/j.2041-1294.2012.00095.x.

[58] P. Wang, Y. Sun, X. Shi, H. Shen, H. Ning, H. Liu, 3D printing of tissue engineering scaffolds: a focus on vascular regeneration, Bio-Des. Manuf. 4 (2021) 344–378, https://doi.org/10.1007/s42242-020-00109-0.

[59] C.M. Murphy, F.J. O'Brien, Understanding the effect of mean pore size on cell activity in collagen-glycosaminoglycan scaffolds, Cell Adhes. Migrat. 4 (2010) 377–381, https://doi.org/10.4161/cam.4.3.11747.

[60] A. Díaz-Arca, P. Ros-Tárraga, M.J.M. Tomé, A.H. De Aza, L. Meseguer-Olmo, P. Mazón, P.N. De Aza, Micro-/Nano-Structured ceramic scaffolds that mimic natural cancellous bone, Materials 14 (2021) 1439, https://doi.org/10.3390/ma14061439.

[61] M.P. Nikolova, M.S. Chavali, Recent advances in biomaterials for 3D scaffolds: a review, Bioact. Mater. 4 (2019) 271–292, https://doi.org/10.1016/j.bioactmat.2019.10.005.